Oblique convergence causes both thrust and strike-slip ruptures during the 2021 M 7.2 Haiti earthquake

Ryo Okuwaki[1,2,3] **& Wenyuan Fan**[4]

[1]Mountain Science Center, University of Tsukuba, Tsukuba, Ibaraki 305-8572, Japan
[2]Faculty of Life and Environmental Sciences, University of Tsukuba, Tsukuba, Ibaraki 305-8572, Japan
[3]COMET, School of Earth and Environment, University of Leeds, Leeds LS2 9JT, UK
[4]Scripps Institution of Oceanography, UC San Diego, La Jolla, California 92093, USA

Key Points:

- The M 7.2 2021 Haiti earthquake sequentially ruptured two disconnected thrust and strike-slip faults
- Neither the thrust or strike-slip fault aligns with the Enriquillo-Plantain Garden fault configuration
- Faulting variability of the earthquake likely reflects the complex deformation partition at the tectonic boundary

Corresponding author: Ryo Okuwaki, `rokuwaki@geol.tsukuba.ac.jp`

Abstract

A devastating magnitude 7.2 earthquake struck Southern Haiti on 14 August 2021. The earthquake caused severe damages and over 2000 casualties. Resolving the earthquake rupture process can provide critical insights into hazard mitigation. Here we use integrated seismological analyses to obtain the rupture history of the 2021 earthquake. We find the earthquake first broke a blind thrust fault and then jumped to a disconnected strike-slip fault. Neither of the fault configurations aligns with the left-lateral tectonic boundary between the Caribbean and North American plates. The complex multi-fault rupture may result from the oblique plate convergence in the region that the initial thrust rupture is due to the boundary-normal compression and the following strike-slip faulting originates from the Gonâve microplate block movement, orienting towards the SW-NE direction. The complex rupture development of the earthquake suggests that the regional deformation is accommodated by a network of segmented faults with diverse faulting conditions.

Plain Language Summary

On 14 August 2021, a devastating magnitude 7.2 earthquake struck Southern Haiti, causing over 2000 casualties and severe infrastructure damages. Southern Haiti situates in between the Caribbean and North American plates, where they converge obliquely at the boundary. The relative motion displaces the plates horizontally and accumulates stress along a major left-lateral fault network. The oblique plate motion also causes an uplift of the region due to the boundary-normal compression. Therefore, earthquakes in the region rupture in complex ways. However, the physical relations between the tectonic regime and the earthquake rupture development are poorly understood, posing challenges to local risk management. Here we use global seismic records to resolve the rupture history of the 2021 Haiti earthquake. We find the earthquake composed of two distinct rupture episodes: a reverse faulting subevent near the epicenter and a strike-slip faulting subevent further west. Both subevents ruptured faults that deviate away from the left-lateral geometry of the Enriquillo-Plantain Garden fault zone. Our results show that the complex tectonic setting of the convergence boundary is imprinted in a segmented fault network with various distinct faulting styles, which may have been influenced by the local small-scale plate fragmentation.

Introduction

Haiti locates in a transpressive tectonic boundary that is seismically active and prone to damaging earthquakes (Manaker et al., 2008; Saint Fleur et al., 2015; Benford et al., 2012) (Fig. 1). The Caribbean plate obliquely converges to the North American plate at 19–20 mm yr^{-1} towards the northeast. The plate motions are largely accommodated by the Septentrional fault zone in the north and the Enriquillo-Plantain Garden fault (EPGF) zone in the south, forming the intermediate Gonâve microplate (Mann et al., 1984; Prentice et al., 2010) (Fig. 1). The oblique convergence results in compressional uplifts in Hispaniola (Haiti and Dominican Republic) in addition to the dominant left-lateral plate movements (Pubellier et al., 2000; Mann et al., 1995). Such a complex tectonic setting drives the development of a intertwined fault system, involving blind secondary faults and segmented faults with various geometries (Jackson et al., 2006; Hayes et al., 2010; Hamling et al., 2017). These faults do not always align with the apparent plate motions and can be missed from geological surveys and geodetic measurements, leading to unexpected complex earthquakes, such as the moment magnitude (M_{W}) 7.0 2010 Haiti earthquake (Hayes et al., 2010; Saint Fleur et al., 2015, 2020).

On 14 August 2021, a devastating M_{W} 7.2 earthquake struck the Tiburon Peninsula, Haiti, ~96 km west of the 2010 earthquake (Fig. 1). The earthquake has caused at least 2000+ casualties and severe infrastructural damages in densely populated areas (reported by the Haitian Civil Protection, Emergency Response Coordination Centre, 2021). The U.S. Geological Survey (USGS) National Earthquake Information Center (NEIC) reported the earthquake origin on 2021-08-14 12:29:08 (UTC) at 18.408°N, 73.475°W, ~125 km west from Port-au-Prince capital city (U.S. Geological Survey Earthquake Hazards Program, 2017). The Global Centroid Moment Tensor (GCMT) solution suggests an oblique strike-slip faulting style of the 2021 Haiti earthquake (Dziewonski et al., 1981; Ekström et al., 2012). The interferometric synthetic aperture radar (InSAR) shows uplift co-seismic deformation near the epicenter and north of EPGF (Geospatial Information Authority of Japan, 2021). The satellite images also suggest westward deformations ~60 km west of the epicenter (Geospatial Information Authority of Japan, 2021). The complex crustal deformation suggests a possible multi-fault rupture of the 2021 Haiti earthquake, which faulting geometries do not seem to align with the main EPGF configuration (Fig. 1).

We investigate the rupture evolution of the 2021 Haiti earthquake by performing integrated seismological analyses, including teleseismic finite-fault inversion and *P*-wave back-projection. Our methods require minimal assumptions of the earthquake rupture propagation. Here we find the earthquake cascadingly ruptured at least two disconnected faults with different faulting styles. The earthquake initiated on a blind thrust fault and then jumped onto a strike-slip fault propagating westward from the epicenter. The fault geometries of the two rupture episodes do not align with the superficial lineament of EPGF. The initial thrust slip likely released strains accumulated from the EPGF-normal convergence. The second strike-slip subevent likely ruptured a fault plane 45° counterclockwise of the EPGF strike, agreeing with the oblique block motion oriented at southwest-northeast. Our source models show that the 2021 earthquake did not rupture the main EPGF but broke secondary faults that were previously unrecognized. The results highlight that the plate convergence is accommodated by a complex fault network with diverse faulting styles in addition to the main EPGF.

Materials and methods

Imaging earthquake rupture processes is critical to understanding earthquake-source physics and assessing hazards induced by ground shaking. However, it can be challenging when multiple different faults are involved (Hayes et al., 2010; Meng et al., 2012; Ulrich et al., 2019). For example, finite-fault inversion often preassumes a fault plane, which limits identifying hidden earthquake rupture processes of different focal mechanisms. The prior information (assumptions) about the fault system may often be inaccurate and differ from the true rupture faults at depth. Such assumption-induced errors can be significant for remote earthquakes when other geophysical and geological observations are limited. Therefore, exploring seismic records with minimal assumptions is highly desirable for uncovering complex earthquake rupture processes.

To analyze the rupture evolution of the 2021 Haiti earthquake, we use a time-domain back-projection method (Ishii et al., 2005; Fan & Shearer, 2015) and a new finite-fault inversion approach (Yagi & Fukahata, 2011; Shimizu et al., 2020). We take advantage of both low- and high-frequency seismic records of globally distributed networks and arrays. The back-projection method is effective at resolving coherent earthquake high-frequency radiation and can identify possible multiple rupture episodes of large earthquakes across complex fault systems with minimal assumptions (Yao et al., 2011; Meng et al., 2012; Satriano et al., 2012; Nissen et al., 2016; D. Wang et al., 2016; Lay et al., 2018; Kehoe & Kiser, 2020). Therefore, it has been successfully implemented to study the spatiotemporal evolution of complex earthquakes, including multi-fault rupture and supershear rupture earthquakes (e.g., Meng et al., 2012; Fan et al., 2016; Hicks et al., 2020). To resolve the earthquake slip distribution, we apply a finite-fault inversion method that is based on the potency-density tensor approach (Shimizu et al., 2020). We directly resolve the fault geometry by representing the fault slip as the superposition of five-basis double couple components (Kikuchi & Kanamori, 1991) and can obtain a spatiotemporal distribution of the potency density (Ampuero & Dahlen, 2005). The method is particularly suitable for investigating the 2021 Haiti earthquake as it can flexibly accommodate rupture scenarios involving multiple faults with various geometries. Further, the method explicitly introduces an error term of Green's function into the data covariance matrix to account for the associated uncertainties (Yagi & Fukahata, 2011). Such a formulation advances the conventional finite-fault inversion by avoiding modeling errors due to fault geometry assumptions and has proven valuable in resolving complex large earthquakes (Okuwaki et al., 2020; Tadapansawut et al., 2021; Hicks et al., 2020; Yamashita et al., 2021). The obtained slip models have illuminated previously unknown fault geometries and sporadic rupture propagations in geometrically complex fault systems (Tadapansawut et al., 2021; Yamashita et al., 2021). Our integrated strategy of earthquake-source imaging is designed to resolve the rupture evolution without assuming the rupture speed, rupture direction, or fault geometry.

Back-projection

We use vertical-component teleseismic P waveforms from globally distributed arrays (839 stations within 30° to 90° epicentral distance) for the back-projection analysis to image the rupture propagation (Fig. S1). We filter the records at 0.2 to 1 Hz with a second-order Butterworth filter. For a data quality-control step, records with signal-to-noise ratios (SNR) less than 5 are removed. The SNR is defined as the root-mean-square (RMS) amplitude ratio from time windows 20 s before and 20 s after the theoretical P-wave arrival obtained from IASP91 (B. Kennett & Engdahl, 1991). We further discard stations that are close to the GCMT nodal planes, and the remaining traces are visually examined to assure clear P wave onsets. The travel time errors due to the 3D velocity structure are corrected by aligning initial P waves with multi-channel cross-correlations of the waveforms within −1 s to 8 s of the theoretical arrivals. We only use records with positive P-wave polarities and average cross-correlation coefficients greater than 0.6 to image the earthquake. We grid potential sources at a 10-km horizontal spacing with the grids fixed at the hypocentral depth, covering a 600 km by 600 km area with its epicenter at the center of the grids. Back-projection images are obtained through the Nth root stacking method (Rost & Thomas, 2002; Xu et al., 2009) with $N = 4$. The Nth root method can sharpen the back-projection images but would distort the absolute amplitude of the stacks (Rost & Thomas, 2002; Xu et al., 2009). Seismic records are self-normalized and inversely scaled by the number of contributing stations within 5°. Such a procedure can neutralize the radiation pattern effects and balance the spatial coverage of stations. To evaluate the rupture propagation, we compute back-projection snapshots with a 10-second stacking window at a 5-second step for five time windows (Fig. 1). These snapshots are normalized by the maximum power of each window (Fig. 1).

The globally distributed arrays maximize the azimuthal coverage of the earthquake, allowing a high spatial resolution of the back-projected results (Fan & Shearer, 2015). We have considered possible biases from the depth and water phases, but such effects would be minor in our results because the earthquake was shallow and we use a long stacking window, and the results are located far away from the coast (Fan & Shearer, 2015, 2018). The robustness of the back-projection results is quantitatively evaluated by a Jackknife re-sampling exercise (Efron & Tibshirani, 1994; Fan & Shearer, 2016) (Fig. 3). The spatial uncertainties of the peak loci are less than 50 km along latitude and 11 km along longitude (Fig. 1 and 3). The spatial uncertainties along the strike (268° azimuth) show that the seismic radiations are well resolved to track the rupture-front migration (Fig. 3).

Finite-fault Inversion

Our finite-fault inversion method is based on a potency-density tensor approach (Shimizu et al., 2020). We use vertical-component teleseismic P waveforms from 43 globally distributed stations (Fig. S2). The data are procured to ensure good azimuthal coverage of high-quality records, which signal-to-noise ratios are sufficient for reliable picks of the P-wave first motions (Okuwaki et al., 2016). The first motions are manually determined. The data are then deconvolved from instrument responses into velocity time series at a 0.6 s sampling interval. To obtain Green's functions, we used the ak135 model (B. L. Kennett et al., 1995) to calculate travel time, ray parameter, and geometric spreading factors. Green's functions are calculated based on a method of the ray-theory approach (Kikuchi & Kanamori, 1991). The CRUST1.0 model (Laske et al., 2013) is used to extract a one-dimensional layered velocity model near the source region to calculate Haskel propagator in Green's functions. We do not apply a low-pass filter to either the observed or synthetic waveforms, and we intend to retrieve detailed rupture processes recorded in the high-frequency components of the seismic records (Shimizu et al., 2020).

Guided by available seismological and geodetic observations (U.S. Geological Survey Earthquake Hazards Program, 2017; Dziewonski et al., 1981; Ekström et al., 2012), we design a planer model domain for the finite-fault inversion (Fig. 1). The model space extends along 268° in strike and 64° in dip directions and covers an area of 170-km in length and 35-km in width. To evaluate possible errors that may arise from the model-domain geometry, we also test alternative geometries adopting a 90° or 0° dipping planer domain (Fig. S3) (see Results section). Each sub-fault is separated by 10 km and 5 km along the strike and dip directions, respectively. The slip-rate function for each source grid is represented by linear B-splines at a temporal interval of 0.6 s. The total source duration is set as 30 s. The maximum rupture velocity is set as 5 km/s, which is guided by the back-projection results (Fig. 3). We set the hypocenter at 18.408°N, 73.475°W, and 12-km at depth for the initial rupture point, based on the earthquake origin reported by USGS NEIC (U.S. Geological Survey Earthquake Hazards Program, 2017). After obtaining a preferred finite-fault model, we evaluate the resolvability of the preferred model by using synthetic waveforms from the solution of the 2021 Haiti earthquake (Figs. 1–3) to invert for a slip model. The results show that the input and output models agree well (Fig. S4), suggesting that the data coverage is sufficient, the inversion is stable, and our obtained finite-fault model of the 2021 Haiti earthquake is robust.

Results

The back-projection images suggest an apparent unilateral westward rupture propagation of the 2021 Haiti earthquake, involving two discrete episodes of strong seismic radiations (0.2–1 Hz). During the first 10 s, we observe the rupture centers near the epicenter with a minor horizontal migration of ~10 km eastward of the epicenter (Fig. 3). Another episode of strong seismic radiations occurs 15 s later and is 60 km westward from the epicenter. The rupture front continued propagating westward till 90 km away from the epicenter lasting for a total of ~30 s (Fig. 1). Intriguingly, there is an apparent spatial gap between the two high-frequency episodes, spanning about 60 km horizontally (Fig. 1). Given that we use a 10 s long stacking time window with a 5 s overlapping time step, this apparent gap is likely real and may represent two distinct subevents. We have tested time windows of various lengths, and this sporadic feature remains the same.

The finite-fault model finds two major slip patches, one centered near the epicenter and the other 70 km west of the epicenter (Fig. 1). The first slip patch is dominated by a reverse faulting mechanism near the epicenter. The resolved focal mechanisms suggest a fault plane striking along the east-west direction with a dipping angle of ~63°. The model domain with the final slip over 1.3 m extends about 40 km by 30 km. This episode of slip released 35% of the total seismic moment for about 10 seconds centers at a depth of 20 km. The second major slip patch has a vertically dipping, strike-slip faulting mechanism. The dominant strike is 223° or 313°, and the slip area covers an area of 40 km in length and 25 km in width of the model domain. Most slips of the second episode occurred from 12 s to 22 s at a depth shallower than ~20-km, releasing 32% of the total seismic moment. The two major slip patches and their disparate mechanisms are robust despite choices of the model domain configuration (Fig. S3). We have tested using a purely vertical or horizontal dipping planer domain, and the main slip features remain the same as of our preferred model (Fig. S3). The total seismic moment of the finite-fault model is 1.3×10^{22} N m (M_W 7.3) for the 2021 Haiti earthquake.

The back-projection and finite-fault models collectively show that the 2021 Haiti earthquake involves at least two discrete rupture episodes, E1 and E2 (Figs. 2 and 3). For the first 10 s of the rupture, the first slip episode (E1) compactly broke a thrust fault within 20 km of the hypocenter. The back-projection images suggest an apparent slow horizontal rupture speed of 1–2 km/s (along 268° azimuth), and the finite-fault model shows that the slip of E1 extends to 25 km at depth. These results suggest that the along dip rupture likely controls this episode. After a temporary hiatus (8 to 12 s) of slip propagation, the second episode (E2) suddenly starts in the western part of the model domain (60 km away from the epicenter, Fig. 3). The horizontal rupture speed of E2 is 4–5 km/s (along 268° azimuth), much faster than that of E1. The moment release starts to decelerate after ~20 s and ceases at ~25 s. Our source models show different faulting styles of E1 and E2 and resolve a clear separation of the two subevents in both space and time.

Discussion

Thrusting faulting of E1 reflecting the oblique plate convergence

The 2021 Haiti earthquake shows a two-stage, multi-segment rupture process involving both thrust and strike-slip faulting styles. The rupture process is unexpected as there is no indication of permitting such a complex evolution from the surface expression of EPGF. The seismic data strongly requires E1 to have a reverse faulting style, a blind thrust fault (Fig. S5). InSAR images show an uplift deformation north of EPGF (Geospatial Information Authority of Japan, 2021), and the aftershocks (up to 1 month) also cluster in the northern side of EPGF (Fig. 1). Although it is difficult to identify the fault plane solely from the finite-fault model, multiple lines of geophysical evidence suggest a north-dipping fault plane of E1, striking the east-west direction.

The majority of E1's moment is released at a deeper region. Assuming the earthquake initiated at 12 km depth (close to the USGS origin), the finite-fault model indicates E1 migrating from shallow (12 km) to deep (25 km) for the first 10 s, rupturing downward within a compact region. The downward rupture propagation corroborates the temporal horizontal stagnation of E1 shown in the back-projection results.

Such a rupture scenario would explain the subtle surface deformation imaged by InSAR near the epicenter.

The thrust faulting style of E1 contrasts the left-lateral strike-slip system of EPGF, illuminating a blind fault releasing compressional strains, which is not registered in the Styron et al. (2020) active fault database. Intriguingly, the E1 rupture area coincides with a region with steep topography near the edge of the l'Asile basin, which is filled with Miocene units upon the Cretaceous fold units (Wessels et al., 2019). The E1 strike aligns with a high topographic trend of the region along the east-west direction. Additionally, the Global Positioning System (GPS) velocity modeling (Benford et al., 2012; Calais et al., 2016) shows that the oblique plate convergence is partitioned into an EPGF-parallel motion at 8.7 mm yr^{-1} and an EPGF-normal motion at 6.0 mm yr^{-1} (Wessels et al., 2019). Therefore, we speculate that E1 reflects a faulting process that uplifts and shortens the crust in the l'Asile region corresponding to the EPGF-normal compression (Fig. 4). Such a faulting process at an oblique transpressive tectonic boundary would have contributed to the development of the topographic feature, leading to folding and thrusting that have been documented by geological surveys (Wessels et al., 2019).

To the east of the l'Asile basin, there was a destructive earthquake in 1770 near the 2021 Haiti earthquake (Fig. 1), of which rupture process is poorly constrained (Calais et al., 2010; Bakun et al., 2012). If the 1770 earthquake released most of the accumulated strains, then there would be a slip deficit amounting to ∼2 m since the last event. E1 of the 2021 Haiti earthquake only slipped about 0.3 m along the EPGF parallel direction, suggesting the remaining slip deficit to be accommodated by future earthquakes in the l'Asile region.

Strike-slip faulting of E2 deviating away from the main EPGF strand

E2 ruptured a vertical strike-slip fault and lasted for about 13 s (from 12 to 25 s). The E2 strike is likely either at a ∼223° (southwest) or ∼313° (northwest) azimuth suggested by the finite-fault model. The back-projection images show a southwestward rupture propagation, favoring the ∼223° strike-slip fault. This strike direction differs from the major trend of EPGF, which orients at a ∼268° azimuth. The inter-seismic GPS velocity fields suggest an obliquely convergent direction along northeast-southwest direction (∼50° azimuth) between the Gonâve microplate and the Caribbean plate (Benford et al., 2012; Calais et al., 2016) (Fig. 4). Such a deformation pattern opposes that the accumulated strains can be released purely by the strike-slip motion along EPGF at the ∼268° direction, but suggests that part of the elastic strains are partitioned at the EPGF-normal direction.

Given the relative plate motion, it is not surprising that E2 ruptured a fault plane rotated counterclockwise from the EPGF strike to the northeast-southwest direction (∼223° azimuth), and we interpret it as a direct consequence of the oblique plate convergence. The topographic feature around the 2021 Haiti earthquake transitions from the l'Asile basin (near E1) to the Macaya mountain (near E2, peak elevation 2347 m), which are connected by the Clonard and Camp-Perrin basins (Saint Fleur et al., 2020) (Fig. 4). Within the EPGF system, the fault strike veers counterclockwise from the l'Asile basin to Camp-Perrin basin. The veering likely formed the left-step of EPGF at ~74°W, which resultant pull-apart motion could have formed the basins. Such a tectonic setting would create faults with various geometries but with limited spatial extents as the whole fault network is confined within 110 km. The intertwined fault network may rupture at once, leading to complex, sporadic rupture developments, such as the 2021 Haiti earthquake.

We observe a strong seismic radiation episode at the western end of E2 from 20 to 30 s. The finite-fault model shows that the focal mechanisms of this last episode (20–30 s) slightly differ from those of slips from 15 to 20 s (Fig. 3). The 20–30 s slips remain as strike-slip ruptures, but their nodal planes rotated about ~10° clockwise at a ~233° azimuth (Fig. 3). If this geometric variation holds true, the fault rotation can serve as a restraining bend (Bruhat et al., 2016), which may have caused a sudden deceleration of the rupture and generated stopping phases, radiating strong high-frequency seismic energies (Madariaga, 1977; Bernard & Madariaga, 1984; Spudich & Frazer, 1984; Okuwaki & Yagi, 2018).

Faulting interaction and triggering of large earthquakes in Haiti

Disconnected faults can interact and trigger each other in various ways during either a single event or an earthquake sequence (Harris et al., 1991, 2002; Nissen et al., 2016; Ruppert et al., 2018; Freed, 2005; Fan & Shearer, 2016; Goldberg et al., 2020). The spatiotemporal correlation of E1 and E2 during the 2021 Haiti earthquake suggests that E1 triggered E2 instantaneously in a complex fault network. To investigate the triggering mechanism, we calculate the static Coulomb failure stress changes (King et al., 1994; Lin & Stein, 2004; Toda et al., 2005; J. Wang et al., 2021) on faults with the E2 geometry from the E1 rupture (Fig. S6). Modeling parameters are detailed in the supplement. We find minor Coulomb stress changes (<20 kPa at 10 km) near the E2 domain (Fig. S6). The stress changes are positive and may have brought the fault closer to failure. However, such an impact would be marginal given the small perturbation values (<20 kPa), suggesting that the static stress change from E1 was unlikely the sole nucleation cause of E2.

The E1 and E2 fault segments are separated by ~60 km and ruptured sequentially within 10 s (Fig. 1), leading to an apparent migration speed of ~6 km/s, which is comparable to the local P-wave velocity in Southern Haiti (Douilly et al., 2013, 2016). In conjunction with the minor effects from the static stress changes, such a spatiotemporal gap during the 2021 Haiti earthquake indicates that the discontinuous jump from E1 to E2 may have been caused by the dynamic effects from the passing seismic waves. We also test the Coulomb stress effects of E1 on the western strand of EPGF. We find greater static stress changes in this case comparing to the E2 case when assuming a target fault with a left-lateral strike-slip geometry along EPGF (Fig. S6). This further confirms the importance of the dynamic effects as an EPGF strand should have slipped if the static stress change was the key driving factor.

The 2021 Haiti earthquake locates ~96 km apart from the 2010 Haiti earthquake, and both earthquakes involve blind thrust faults in a similar fashion (Hayes et al., 2010). The correlation raises the question of whether the 2010 earthquake triggered the 2021

Haiti earthquake. Such an earthquake-to-earthquake triggering process has been reported at various tectonic settings, and the 1992 Landers earthquake and the 1999 Hector Mine earthquake in southern California resemble a similar pair to the Haiti earthquakes (e.g., Parsons & Dreger, 2000; Felzer et al., 2002; Pollitz & Sacks, 2002). Both the Landers and the Hector Mine earthquakes are strike-slip events involving multiple segments with similar magnitudes of the Haiti earthquakes, and the Landers earthquake likely triggered the Hector Mine earthquake after eight years with static stress changes playing an important role in its nucleation (e.g., Pollitz & Sacks, 2002; Price & Burgmann, 2002; Zeng, 2001). Here we calculate the Coulomb stress changes on the E1 fault induced by the 2010 Haiti earthquake (Hayes et al., 2010) (Fig. S7). The result shows positive Coulomb stress perturbations near the 2021 hypocenter, but the stress changes are negligible at a 12 km depth as <10 kPa (see the supplement for modeling details). Our model of simple Coulomb stress interactions does not predict an obvious causal relationship between the two earthquakes (Fig. S7). Intriguingly, the 2010 Haiti earthquake would cause a greater static stress perturbation at the 2021 hypocenter if the receiver fault shares the EPGF geometry (Fig. S7). We speculate that the static stress changes alone from the 2010 Haiti earthquake are unlikely to enable the failure (E1) of the 2021 Haiti earthquake.

Conclusions

We identify two distinct rupture episodes of the M_{W} 7.2 2021 Haiti earthquake. In the first episode, E1 ruptured a blind thrust fault, and the earthquake then jumped to a strike-slip fault (E2) that is 60 km west of the epicenter. The complex rupture process likely results from the regional oblique plate convergence. Further, the first episode may have only released part of the accumulated strain since the last damaging earthquake in 1770, suggesting future hazards of the area. The second subevent strikes at a direction differing from the EPGF network trend. Its southwest-northeast strike orientation reflects the oblique convergence motion between the Caribbean plate and the Gonâve microplate. The discontinuous jump from E1 to E2 ruptures is likely facilitated by dynamic triggering. The adjacent 2010 Haiti earthquake caused minor (<10 kPa) Coulomb stress changes in the 2021 rupture area, excluding an obvious cause-and-effect relation due to the static stress changes between the two earthquakes. The complex tectonic setting produces multiple-segmented fault patches that have various focal mechanisms, and the 2021 Haiti earthquake exemplifies that these fault patches may rupture at once, causing devastating hazards over a large region.

Data Availability Statement

All the materials presented in this paper are archived and available at https://doi.org/10.5281/zenodo.5534984. The seismic data were downloaded through the IRIS Wilber 3 system (https://ds.iris.edu/wilber3/find_event) or IRIS Web Services (https://service.iris.edu). We used ObsPy (https://doi.org/10.5281/zenodo.165135; Beyreuther et al., 2010), Pyrocko (https://pyrocko.org/; The Pyrocko Developers, 2017), matplotlib (https://doi.org/10.5281/zenodo.592536; Hunter, 2007), Generic Mapping Tools (https://doi.org/10.5281/zenodo.3407865; Wessel & Luis, 2017); and Scientific colour maps (https://

doi.org/10.5281/zenodo.1243862; Crameri, 2018; Crameri et al., 2020) for data processing and visualization. `AutoCoulomb` package (J. Wang et al., 2021) is used for Coulomb stress analysis, which is available at https://github.com/jjwangw/CoulombAnalysis.

Acknowledgments

We thank the editors and reviewers for their evaluations. The facilities of IRIS Data Services, and specifically the IRIS Data Management Center, were used for access to waveforms, related metadata, and/or derived products used in this study. IRIS Data Services are funded through the Seismological Facilities for the Advancement of Geoscience (SAGE) Award of the National Science Foundation under Cooperative Support Agreement EAR-1851048. The authors declare no conflicts of interest relevant to this study. W.F. acknowledges support from NSF grant EAR-2022441. We thank Tim J. Wright for fruitful discussions.

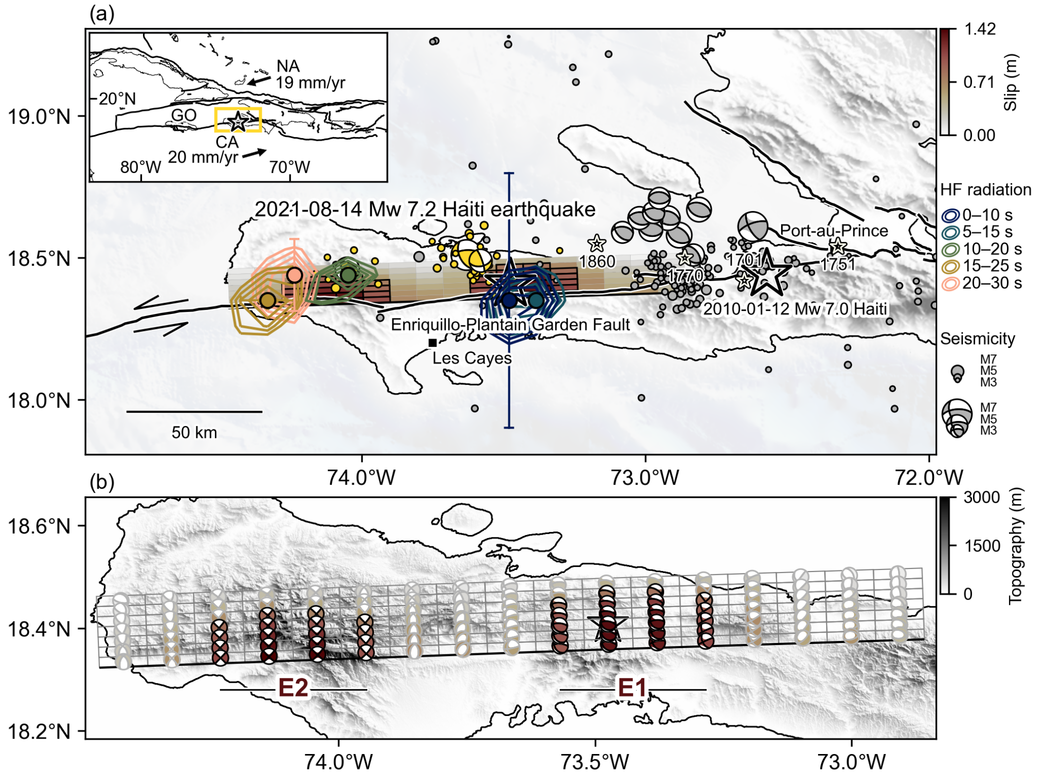

Figure 1. Finite-fault and back-projection models of the 2021 Haiti earthquake and seismotectonic summary of the Tiburon Peninsula, Southern Haiti. (a) The colored cells show the finite-fault solution. Large slip patches (>50% of the maximum slip) are empathized by black cell boarders. The colored contours show the back-projection results. The location uncertainties (one standard deviation of latitude or longitude) are from a Jackknife re-sampling exercise. The black stars show the epicenters of the 2021 and 2010 Haiti earthquakes (U.S. Geological Survey Earthquake Hazards Program, 2017). The white stars show historical earthquakes in the region (Bakun et al., 2012). The gray dots are the background seismicity, and the yellow dots are the 1-month aftershocks of the 2021 Haiti earthquake. The gray and yellow beach balls show available GCMT solutions of the events (Dziewonski et al., 1981; Ekström et al., 2012) before and after the 2021 Haiti earthquake. The black lines show active faults in the region (Styron et al., 2020). The inset shows regional tectonics (yellow rectangle, Fig. 1a) with the black lines as the plate boundaries (Bird, 2003) and the arrow showing the relative plate velocity vector between the Caribbean (CA) and the North American (NA) plates (DeMets et al., 2010) juxtaposed against the Gonâve (GO) microplate. The star shows the epicenter of the 2021 Haiti earthquake. The topography/bathymetry is from GEBCO Bathymetric Compilation Group 2019 (2019). (b) Our finite-fault solution. The beach balls show the lower-hemisphere projections of the moment tensor solutions of the subfaults. Large slip areas (>50% of the maximum slip) are empathized by black lines. The topography is from Shuttle Radar Topography Mission (U.S. Geological Survey, 2015).

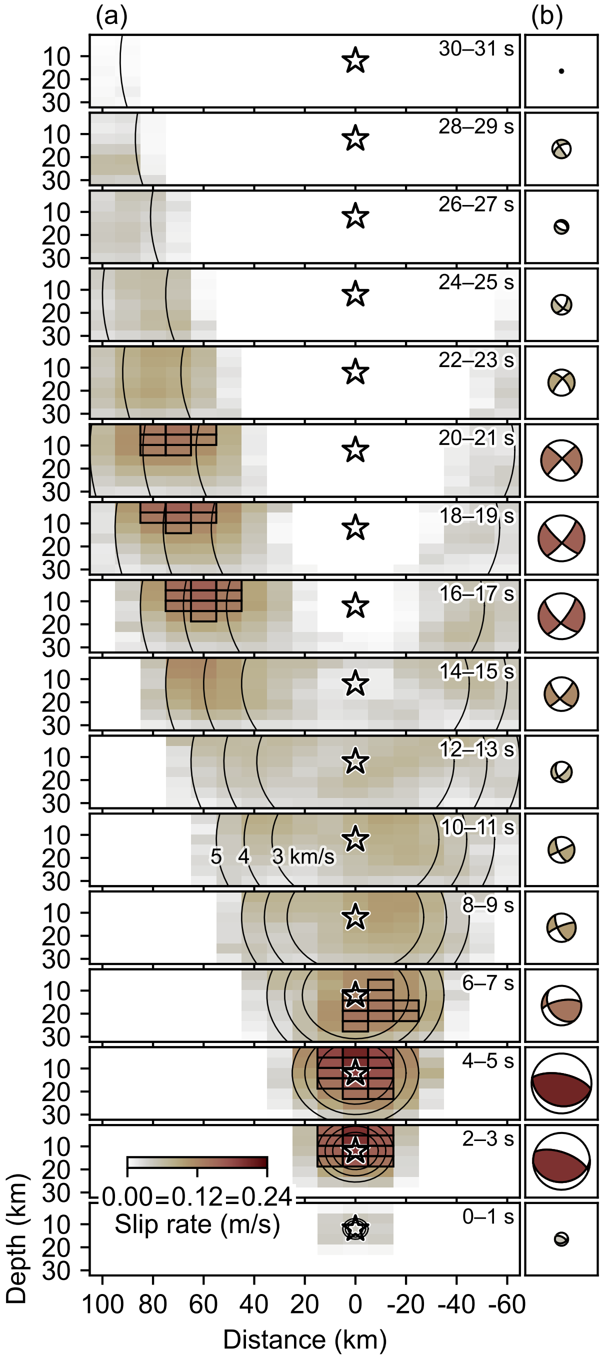

Figure 2. Snapshots of the finite-fault model. (a) The cross section of the slip-rate distribution. Large slip rate areas (>50% of the maximum slip rate) are outlined by the black cell boarders. The star denotes the hypocenter. The black circles are the reference rupture speeds. (b) Centroid moment tensor solutions of the finite-fault model for the snapshot time windows. The color and size of the focal mechanisms correlate with the maximum slip rates of the time windows.

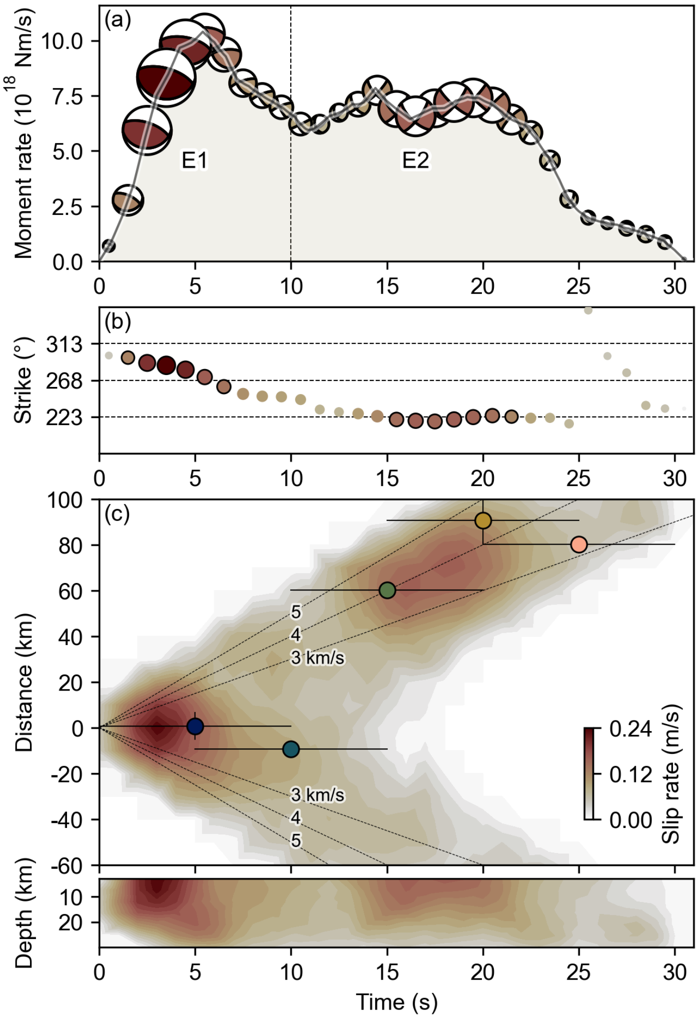

Figure 3. Spatiotemporal evolutions of the finite-fault and back-projection models. (a) Moment rate function of the finite-fault model. The beach balls show the centroid moment tensor solutions of the finite-fault model for the snapshot time windows of every 1 s. The color and size of the focal mechanisms correlate with the maximum slip rates of the time windows. (b) Strikes of the centroid moment tensor solutions shown in Fig. 3a. As reasoned in the paper, we prefer a north-dipping fault plane for E1 from 0–10 s and a southwest-northeast fault plane for E2 from 15–25 s. The color and size of the circles correlate with the maximum slip rates of the time windows with large slip rate snapshots (>50% of the maximum slip rate) outlined by black circles. (c) Spatiotemporal distribution of the finite-fault model and the back-projection peak loci of the five 10-s long windows. The results are projected along a direction of 268° azimuth (middle panel) and along depth (bottom panel, back-projection has no depth resolution for this case). The contours show the slip rate distributions. The colored dots are the back-projection peak loci of the 10-s long snapshots (Fig. 1). The vertical bars are the uncertainty estimates from the jackknife re-sampling exercise and the horizontal bars show the stacking window length. The black lines show the reference rupture speeds.

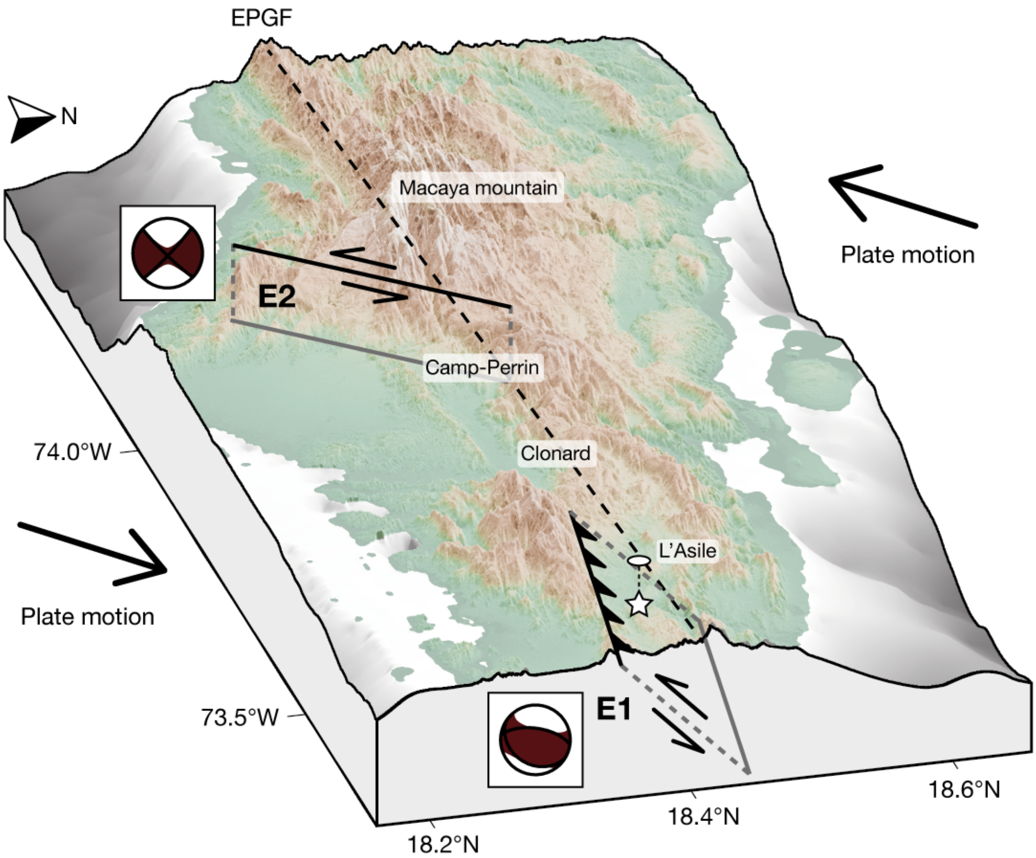

Figure 4. Cartoon interpretation of the faulting process and the cascading rupture development of the 2021 Haiti earthquake. The star shows the hypocenter (U.S. Geological Survey Earthquake Hazards Program, 2017). The one-side arrows show the interpreted fault motions. The beach balls are the centroid moment tensor solutions of the two rupture episodes (E1 and E2, Fig. 1). The solid black lines show the surface projections of faults. The dashed line shows the EPGF trace (268° azimuth). The full arrows show the relative plate motion direction of the Caribbean and Gonâve plates (Benford et al., 2012). The topography is from Shuttle Radar Topography Mission (U.S. Geological Survey, 2015).

References

Ampuero, J.-P., & Dahlen, F. A. (2005). Ambiguity of the Moment Tensor. *Bull. Seism. Soc. Am.*, *95*(2), 390. doi:10.1785/0120040103

Bakun, W. H., Flores, C. H., & ten Brink, U. S. (2012). Significant earthquakes on the Enriquillo fault system, Hispaniola, 1500-2010: Implications for seismic hazard. *Bull. Seismol. Soc. Am.*, *102*(1), 18–30. doi:10.1785/0120110077

Benford, B., Demets, C., & Calais, E. (2012). GPS estimates of microplate motions, northern Caribbean: Evidence for a Hispaniola microplate and implications for earthquake hazard. *Geophys. J. Int.*, *191*(2), 481–490. doi:10.1111/j.1365-246X.2012.05662.x

Bernard, P., & Madariaga, R. (1984). A new asymptotic method for the modeling of near-field accelerograms. *Bull. Seismol. Soc. Am.*, *74*(2), 539–557. doi:10.1785/bssa0740020539

Beyreuther, M., Barsch, R., Krischer, L., Megies, T., Behr, Y., & Wassermann, J. (2010). ObsPy: A Python Toolbox for Seismology. *Seismol. Res. Lett.*, *81*(3), 530–533. doi:10.1785/gssrl.81.3.530

Bird, P. (2003). An updated digital model of plate boundaries. *Geochemistry, Geophys. Geosystems*, *4*(3), 1105. doi:10.1029/2001GC000252

Bruhat, L., Fang, Z., & Dunham, E. M. (2016). Rupture complexity and the supershear transition on rough faults. *J. Geophys. Res. Solid Earth*, *121*(1), 210–224. doi:10.1002/2015JB012512

Calais, E., Freed, A., Mattioli, G., Amelung, F., Jónsson, S., Jansma, P., … Momplaisir, R. (2010). Transpressional rupture of an unmapped fault during the 2010 Haiti earthquake. *Nat. Geosci.*, *3*(11), 794–799. doi:10.1038/ngeo992

Calais, E., Symithe, S., Mercier de Lépinay, B., & Prépetit, C. (2016). Plate boundary segmentation in the northeastern Caribbean from geodetic measurements and Neogene geological observations. *Comptes Rendus - Geosci.*, *348*(1), 42–51. doi:10.1016/j.crte.2015.10.007

Crameri, F. (2018). Geodynamic diagnostics, scientific visualisation and StagLab 3.0. *Geosci. Model Dev.*, *11*(6), 2541–2562. doi:10.5194/gmd-11-2541-2018

Crameri, F., Shephard, G. E., & Heron, P. J. (2020). The misuse of colour in science communication. *Nat. Commun.*, *11*(1), 5444. doi:10.1038/s41467-020-19160-7

DeMets, C., Gordon, R. G., & Argus, D. F. (2010). Geologically current plate motions. *Geophys. J. Int.*, *181*(1), 1–80. doi:10.1111/j.1365-246X.2009.04491.x

Douilly, R., Ellsworth, W. L., Kissling, E., Freed, A. M., Deschamps, A., & Mercier de Lépinay, B. (2016). 3-D velocity structure in southern Haiti from local earthquake tomography. *J. Geophys. Res. Solid Earth*, *121*(12), 8813–8832. doi:10.1002/2016JB013123

Douilly, R., Haase, J. S., Ellsworth, W. L., Bouin, M. P., Calais, E., Symithe, S. J., … Hough, S. E. (2013). Crustal structure and fault geometry of the 2010 Haiti earthquake from temporary seismometer deployments. *Bull. Seismol. Soc. Am.*, *103*(4), 2305–2325. doi:10.1785/0120120303

Dziewonski, A. M., Chou, T.-A., & Woodhouse, J. H. (1981). Determination of earthquake source parameters from waveform data for studies of global and regional seismicity. *J. Geophys. Res. Solid Earth*, *86*(B4), 2825–2852.

doi:10.1029/JB086iB04p02825
Efron, B., & Tibshirani, R. (1994). *An Introduction to the Bootstrap*. doi:10.1201/9780429246593
Ekström, G., Nettles, M., & Dziewoński, A. (2012). The global CMT project 2004–2010: Centroid-moment tensors for 13,017 earthquakes. *Phys. Earth Planet. Inter.*, *200-201*, 1–9. doi:10.1016/j.pepi.2012.04.002
Emergency Response Coordination Centre. (2021). *Haiti - Earthquake, update (DG ECHO, GDACS, Copernicus EMS, Haiti Civil Protection).* (https://erccportal.jrc.ec.europa.eu/ECHO-Products/Echo-Flash#/echo-flash-items/21504)
Fan, W., & Shearer, P. M. (2015). Detailed rupture imaging of the 25 April 2015 Nepal earthquake using teleseismic P waves. *Geophys. Res. Lett.*, *42*(14), 5744–5752. doi:10.1002/2015GL064587
Fan, W., & Shearer, P. M. (2016). Local near instantaneously dynamically triggered aftershocks of large earthquakes. *Science*, *353*(6304), 1133–1136. doi:10.1126/science.aag0013
Fan, W., & Shearer, P. M. (2018). Coherent seismic arrivals in the P wave coda of the 2012 Mw 7.2 Sumatra earthquake: Water reverberations or an early aftershock? *J. Geophys. Res. Solid Earth*, *123*(4), 3147–3159. doi:10.1002/2018JB015573
Fan, W., Shearer, P. M., Ji, C., & Bassett, D. (2016). Multiple branching rupture of the 2009 Tonga-Samoa earthquake. *J. Geophys. Res. Solid Earth*, *121*(8), 5809–5827. doi:10.1002/2016JB012945
Felzer, K. R., Becker, T. W., Abercrombie, R. E., Ekström, G., & Rice, J. R. (2002). Triggering of the 1999 Mw 7.1 Hector Mine earthquake by aftershocks of the 1992 Mw 7.3 Landers earthquake. *J. Geophys. Res. Solid Earth*, *107*(B9), ESE–6. doi:10.1029/2001JB000911
Freed, A. M. (2005). Earthquake triggering by static, dynamic, and post-seismic stress transfer. *Annu. Rev. Earth Planet. Sci.*, *33*(1), 335–367. doi:10.1146/annurev.earth.33.092203.122505
GEBCO Bathymetric Compilation Group 2019. (2019). *The GEBCO_2019 Grid - a continuous terrain model of the global oceans and land.* British Oceanographic Data Centre, National Oceanography Centre, NERC, UK. doi:10/c33m
Geospatial Information Authority of Japan. (2021). *The 2021 Haiti Earthquake: Crustal deformation detected by ALOS-2 data.* (https://www.gsi.go.jp/cais/topic20210814-e.html)
Goldberg, D. E., Melgar, D., Sahakian, V., Thomas, A., Xu, X., Crowell, B., & Geng, J. (2020). Complex rupture of an immature fault zone: A simultaneous kinematic model of the 2019 Ridgecrest, CA earthquakes. *Geophysical Research Letters*, *47*(3), e2019GL086382. doi:10.1029/2019GL086382
Hamling, I. J., Hreinsdóttir, S., Clark, K., Elliott, J., Liang, C., Fielding, E., … Stirling, M. (2017). Complex multifault rupture during the 2016 Mw 7.8 Kaikōura earthquake, New Zealand. *Science*, *356*(6334). doi:10.1126/science.aam7194
Harris, R. A., Archuleta, R. J., & Day, S. M. (1991). Fault steps and the dynamic rupture process: 2-D numerical simulations of a spontaneously propagating shear fracture. *Geophys. Res. Lett.*, *18*(5), 893–896. doi:10.1029/91GL01061
Harris, R. A., Dolan, J. F., Hartleb, R., & Day, S. M. (2002). The 1999 İzmit, Turkey,

earthquake: A 3D dynamic stress transfer model of intraearthquake triggering. *Bull. Seismol. Soc. Am.*, *92*(1), 245–255. doi:10.1785/0120000825

Hayes, G. P., Briggs, R. W., Sladen, A., Fielding, E. J., Prentice, C., Hudnut, K., ... Simons, M. (2010). Complex rupture during the 12 January 2010 Haiti earthquake. *Nat. Geosci.*, *3*(11), 800–805. doi:10.1038/ngeo977

Hicks, S. P., Okuwaki, R., Steinberg, A., Rychert, C. A., Harmon, N., Abercrombie, R. E., ... Sudhaus, H. (2020). Back-propagating supershear rupture in the 2016 Mw 7.1 Romanche transform fault earthquake. *Nat. Geosci.*, *13*(9), 647–653. doi:10.1038/s41561-020-0619-9

Hunter, J. D. (2007). Matplotlib: A 2D Graphics Environment. *Comput. Sci. Eng.*, *9*(3), 90–95. doi:10.1109/MCSE.2007.55

Ishii, M., Shearer, P. M., Houston, H., & Vidale, J. E. (2005). Extent, duration and speed of the 2004 Sumatra-Andaman earthquake imaged by the Hi-Net array. *Nature*, *435*(7044), 933–936. doi:10.1038/nature03675

Jackson, J., Bouchon, M., Fielding, E., Funning, G., Ghorashi, M., Hatzfeld, D., ... Wright, T. (2006). Seismotectonic, rupture process, and earthquake-hazard aspects of the 2003 December 26 Bam, Iran, earthquake. *Geophys. J. Int.*, *166*(3), 1270–1292. doi:10.1111/j.1365-246X.2006.03056.x

Kehoe, H., & Kiser, E. (2020). Evidence of a supershear transition across a fault stepover. *Geophys. Res. Lett.*, *47*(10), e2020GL087400. doi:10.1029/2020GL087400

Kennett, B., & Engdahl, E. (1991). Traveltimes for global earthquake location and phase identification. *Geophys. J. Int.*, *105*(2), 429–465. doi:10.1111/j.1365-246X.1991.tb06724.x

Kennett, B. L., Engdahl, E. R., & Buland, R. (1995). Constraints on seismic velocities in the Earth from traveltimes. *Geophys. J. Int.*, *122*(1), 108–124. doi:10.1111/j.1365-246X.1995.tb03540.x

Kikuchi, M., & Kanamori, H. (1991). Inversion of complex body waves-III. *Bull. Seism. Soc. Am.*, *81*(6), 2335–2350. doi:10.1785/BSSA0810062335

King, G. C., Stein, R. S., & Lin, J. (1994). Static stress changes and the triggering of earthquakes. *Bull. Seismol. Soc. Am.*, *84*(3), 935–953. doi:10.1785/BSSA0840030935

Laske, G., Masters, T. G., Ma, Z., & Pasyanos, M. (2013). Update on CRUST1.0 - A 1-degree Global Model of Earth's Crust. *Geophys. Res. Abstr. 15*, *Abstr. EGU2013-2658*, *15*, Abstract EGU2013–2658. (https://igppweb.ucsd.edu/~gabi/crust1.html)

Lay, T., Ye, L., Bai, Y., Cheung, K. F., & Kanamori, H. (2018). The 2018 MW 7.9 Gulf of Alaska Earthquake: Multiple Fault Rupture in the Pacific Plate. *Geophys. Res. Lett.*, *45*(18), 9542–9551. doi:10.1029/2018GL079813

Lin, J., & Stein, R. S. (2004). Stress triggering in thrust and subduction earthquakes and stress interaction between the southern San Andreas and nearby thrust and strike-slip faults. *J. Geophys. Res. Solid Earth*, *109*(B2), 1–19. doi:10.1029/2003jb002607

Madariaga, R. (1977). High-frequency radiation from crack (stress drop) models of earthquake faulting. *Geophys. J. Int.*, *51*(3), 625–651. doi:10.1111/j.1365-246X.1977.tb04211.x

Mai, P. M., & Thingbaijam, K. K. (2014). SRCMOD: An online database of finite-fault rupture models. *Seismol. Res. Lett.*, *85*(6), 1348–1357. doi:10.1785/0220140077

Manaker, D. M., Calais, E., Freed, A. M., Ali, S. T., Przybylski, P., Mattioli, G., ... De Chabalier, J. B. (2008). Interseismic plate coupling and strain partitioning in the Northeastern Caribbean. *Geophys. J. Int.*, *174*(3), 889–903. doi:10.1111/j.1365-246X.2008.03819.x

Mann, P., Burke, K., & Matumoto, T. (1984). Neotectonics of Hispaniola: plate motion, sedimentation, and seismicity at a restraining bend. *Earth Planet. Sci. Lett.*, *70*(2), 311–324. doi:10.1016/0012-821X(84)90016-5

Mann, P., Taylor, F. W., Edwards, R. L., & Ku, T. L. (1995). Actively evolving microplate formation by oblique collision and sideways motion along strike-slip faults: An example from the northeastern Caribbean plate margin. *Tectonophysics*, *246*(1-3), 1–69. doi:10.1016/0040-1951(94)00268-E

Meng, L., Ampuero, J. P., Stock, J., Duputel, Z., Luo, Y., & Tsai, V. C. (2012). Earthquake in a maze: Compressional rupture branching during the 2012 Mw 8.6 Sumatra earthquake. *Science*, *337*(6095), 724–726. doi:10.1126/science.1224030

Nissen, E., Elliott, J. R., Sloan, R. A., Craig, T. J., Funning, G. J., Hutko, A., ... Wright, T. J. (2016). Limitations of rupture forecasting exposed by instantaneously triggered earthquake doublet. *Nat. Geosci.*, *9*(4), 330–336. doi:10.1038/ngeo2653

Okuwaki, R., Hirano, S., Yagi, Y., & Shimizu, K. (2020). Inchworm-like source evolution through a geometrically complex fault fueled persistent supershear rupture during the 2018 Palu Indonesia earthquake. *Earth Planet. Sci. Lett.*, *547*, 116449. doi:10.1016/j.epsl.2020.116449

Okuwaki, R., & Yagi, Y. (2018). Role of geometric barriers in irregular-rupture evolution during the 2008 Wenchuan earthquake. *Geophys. J. Int.*, *212*(3), 1657–1664. doi:10.1093/gji/ggx502

Okuwaki, R., Yagi, Y., Aránguiz, R., González, J., & González, G. (2016). Rupture Process During the 2015 Illapel, Chile Earthquake: Zigzag-Along-Dip Rupture Episodes. *Pure Appl. Geophys.*, *173*(4), 1011–1020. doi:10.1007/s00024-016-1271-6

Parsons, T., & Dreger, D. S. (2000). Static-stress impact of the 1992 Landers earthquake sequence on nucleation and slip at the site of the 1999 m 7.1 Hector Mine earthquake, southern California. *Geophys. Res. Lett.*, *27*(13), 1949–1952. doi:10.1029/1999GL011272

Pollitz, F. F., & Sacks, I. S. (2002). Stress triggering of the 1999 Hector Mine earthquake by transient deformation following the 1992 Landers earthquake. *Bull. Seismol. Soc. Am.*, *92*(4), 1487–1496. doi:10.1785/0120000918

Prentice, C. S., Mann, P., Crone, A. J., Gold, R. D., Hudnut, K. W., Briggs, R. W., ... Jean, P. (2010). Seismic hazard of the Enriquillog-Plantain Garden fault in Haiti inferred from palaeoseismology. *Nat. Geosci.*, *3*(11), 789–793. doi:10.1038/ngeo991

Price, E. J., & Burgmann, R. (2002). Interactions between the Landers and Hector Mine, California, earthquakes from space geodesy, boundary element modeling, and time-dependent friction. *Bull. Seismol. Soc. Am.*, *92*(4), 1450–1469. doi:10.1785/0120000924

Pubellier, M., Mauffret, A., Leroy, S., Vila, J. M., & Amilcar, H. (2000). Plate boundary readjustment in oblique convergence: Example of the neogene of hispaniola, Greater Antilles. *Tectonics*, *19*(4), 630–648. doi:10.1029/2000TC900007

Rost, S., & Thomas, C. (2002). Array seismology: Methods and applications. *Rev. Geophys.*, *40*(3), 1008. doi:10.1029/2000RG000100

Ruppert, N. A., Rollins, C., Zhang, A., Meng, L., Holtkamp, S. G., West, M. E., & Freymueller, J. T. (2018). Complex Faulting and Triggered Rupture During the 2018 MW 7.9 Offshore Kodiak, Alaska, Earthquake. *Geophys. Res. Lett.*, *45*(15), 7533–7541. doi:10.1029/2018GL078931

Saint Fleur, N., Feuillet, N., Grandin, R., Jacques, E., Weil-Accardo, J., & Klinger, Y. (2015). Seismotectonics of southern Haiti: A new faulting model for the 12 January 2010 M7.0 earthquake. *Geophys. Res. Lett.*, *42*(23), 10273–10281. doi:10.1002/2015GL065505

Saint Fleur, N., Klinger, Y., & Feuillet, N. (2020). Detailed map, displacement, paleoseismology, and segmentation of the Enriquillo-Plantain Garden Fault in Haiti. *Tectonophysics*, *778*, 228368. doi:10.1016/j.tecto.2020.228368

Satriano, C., Kiraly, E., Bernard, P., & Vilotte, J.-P. (2012). The 2012 Mw 8.6 Sumatra earthquake: Evidence of westward sequential seismic ruptures associated to the reactivation of a N-S ocean fabric. *Geophys. Res. Lett.*, *39*(15). doi:10.1029/2012GL052387

Shimizu, K., Yagi, Y., Okuwaki, R., & Fukahata, Y. (2020). Development of an inversion method to extract information on fault geometry from teleseismic data. *Geophys. J. Int.*, *220*(2), 1055–1065. doi:10.1093/gji/ggz496

Spudich, P., & Frazer, L. N. (1984). Use of ray theory to calculate high-frequency radiation from earthquake sources having spatially variable rupture velocity and stress drop. *Bull. Seismol. Soc. Am.*, *74*(6), 2061–2082. doi:10.1785/BSSA0740062061

Styron, R., García-Pelaez, J., & Pagani, M. (2020). CCAF-DB: The Caribbean and Central American active fault database. *Nat. Hazards Earth Syst. Sci.*, *20*(3), 831–857. doi:10.5194/nhess-20-831-2020

Tadapansawut, T., Okuwaki, R., Yagi, Y., & Yamashita, S. (2021). Rupture Process of the 2020 Caribbean Earthquake Along the Oriente Transform Fault, Involving Supershear Rupture and Geometric Complexity of Fault. *Geophys. Res. Lett.*, *48*(1), 1–9. doi:10.1029/2020GL090899

The Pyrocko Developers. (2017). *Pyrocko: A Versatile Seismology Toolkit for Python.* doi:10.5880/GFZ.2.1.2017.001

Toda, S., Stein, R. S., Richards-Dinger, K., & Bozkurt, S. B. (2005). Forecasting the evolution of seismicity in southern California: Animations built on earthquake stress transfer. *J. Geophys. Res. Solid Earth*, *110*(5), 1–17. doi:10.1029/2004JB003415

Ulrich, T., Vater, S., Madden, E. H., Behrens, J., van Dinther, Y., van Zelst, I., ... Gabriel, A. A. (2019). Coupled, Physics-Based Modeling Reveals Earthquake Displacements are Critical to the 2018 Palu, Sulawesi Tsunami. *Pure Appl. Geophys.*, *176*(10), 4069–4109. doi:10.1007/s00024-019-02290-5

U.S. Geological Survey. (2015). *Shuttle Radar Topography Mission 1 Arc-Second Global.* doi:10.5066/F7PR7TFT

U.S. Geological Survey Earthquake Hazards Program. (2017). *Advanced National Seismic System (ANSS) Comprehensive Catalog of Earthquake Events and Products.* doi:10.5066/F7MS3QZH

Wang, D., Mori, J., & Koketsu, K. (2016). Fast rupture propagation for large strike-slip earthquakes. *Earth Planet. Sci. Lett.*, *440*, 115–126. doi:10.1016/j.epsl.2016.02.022

Wang, J., Xu, C., Freymueller, J. T., Wen, Y., & Xiao, Z. (2021). AutoCoulomb: An automated configurable program to calculate coulomb stress changes on receiver faults with any orientation and its application to the 2020 Mw7.8 Simeonof Island, Alaska, Earthquake. *Seismol. Res. Lett.*, *92*(4), 2591–2609. doi:10.1785/0220200283

Wessel, P., & Luis, J. F. (2017). The GMT/MATLAB Toolbox. *Geochemistry, Geophys. Geosystems*, *18*(2), 811–823. doi:10.1002/2016GC006723

Wessels, R. J., Ellouz-Zimmermann, N., Bellahsen, N., Hamon, Y., Rosenberg, C., Deschamps, R., … Leroy, S. (2019). Polyphase tectonic history of the Southern Peninsula, Haiti: from folding-and-thrusting to transpressive strike-slip. *Tectonophysics*, *751*, 125–149. doi:10.1016/j.tecto.2018.12.011

Xu, Y., Koper, K. D., Sufri, O., Zhu, L., & Hutko, A. R. (2009). Rupture imaging of the Mw 7.9 12 May 2008 Wenchuan earthquake from back projection of teleseismic P waves. *Geochemistry, Geophys. Geosystems*, *10*(4), Q04006. doi:10.1029/2008GC002335

Yagi, Y., & Fukahata, Y. (2011). Introduction of uncertainty of Green's function into waveform inversion for seismic source processes. *Geophys. J. Int.*, *186*(2), 711–720. doi:10.1111/j.1365-246X.2011.05043.x

Yamashita, S., Yagi, Y., Okuwaki, R., Shimizu, K., Agata, R., & Fukahata, Y. (2021). Consecutive ruptures on a complex conjugate fault system during the 2018 Gulf of Alaska earthquake. *Sci. Rep.*, *11*(1), 5979. doi:10.1038/s41598-021-85522-w

Yao, H., Gerstoft, P., Shearer, P. M., & Mecklenbräuker, C. (2011). Compressive sensing of the Tohoku-Oki Mw 9.0 earthquake: Frequency-dependent rupture modes. *Geophys. Res. Lett.*, *38*(20). doi:10.1029/2011GL049223

Zeng, Y. (2001). Viscoelastic stress-triggering of the 1999 Hector Mine earthquake by the 1992 Landers earthquake. *Geophys. Res. Lett.*, *28*(15), 3007–3010. doi:10.1029/2000GL012806